Root Walker: an automated pipeline for large scale quantification of early root growth responses at high spatial and temporal resolution

Platre Matthieu Pierre[1♫*], Halvorson Zachary[1*], Mehta Preyanka[1], Brent Lukas[1], Gleason F. Matias[1], Faizi Kian[1], Busch Wolfgang[1♫].

[*]author contributed equally

[♫]Correspondence: mplatre@salk.edu, wbusch@salk.edu

[1] Salk Institute for Biological Studies, Plant Molecular And Cellular Biology Laboratory, 10010 N Torrey Pines Rd, La Jolla, CA 92037, USA.

Summary

Plants are sessile organisms that constantly need to adapt to their changing environment. The root is exposed to numerous environmental signals ranging from nutrients and water to microbial molecular patterns. These signals can trigger distinct responses including the rapid increase or decrease of root growth. Consequently, using root growth as a read out for signal perception allows for deciphering which cues root senses and how they integrate it. To date, studies measuring root growth responses using large numbers of roots are often limited either by the lack of high-throughput image acquisition, scalable analysis methods, and by low spatiotemporal resolution. We developed the "Root Walker" pipeline, which utilizes automated microscopes to acquire images of many roots exposed to controlled treatments with high-spatiotemporal-resolution in conjunction with a fast and automated image analysis software. We demonstrate the power of this pipeline by quantifying fast root growth rate responses in the order of minutes upon treatments with natural auxin, and by quantifying slower root growth rate responses in the order of hours upon treatment with two mitogen-associated protein kinase cascade inhibitors. We find a concentration dependent root growth response to auxin and expose the specificity of one MAPK inhibitor for affecting root growth. Overall, the "Root Walker" toolkit is a relevant tool for the plant community to conduct large-scale screening of root growth changes for a variety of purposes including genetic screens for root sensing and response mechanisms.

Introduction

The root is an organ that is involved in a plethora of functions such as anchoring the plant into the soil and nutrient and water uptake. However, resources are not evenly distributed in the soil. Moreover, plants interact with beneficial and pathogenic microorganisms which can promote, limit resources, or pose a threat. It is therefore not surprising that roots can sense and respond to many different cues, ranging from physical cues such as gravity and touch to chemical cues such as water, nutrients or microbially associated molecules (Morris *et al.*, 2017). Root responses to the environment are almost always resulting in a change of root growth. These responses are key for plant adaptation and over time shape the root system architecture (RSA). During the last decade, the root growth has been successfully used to novel genes and

molecular mechanisms that underlie root responses to the environment (Satbhai *et al.*, 2017; Li *et al.*, 2019; Platre *et al.*, 2022). However, these studies have utilized screens on relatively late read outs of root growth change, corresponding to days after exposure to distinct growth environments. Such approaches might not be very powerful to identify sensory mechanisms that are still not yet identified for many environmental cues such as nutrients (Jia, Giehl and von Wirén, 2022). We hypothesized that it might be more powerful to measure responses dynamically during the first hours after transfer to a treatment condition. However, tools to precisely measure such responses on the order of hundreds or thousands of roots with high spatiotemporal resolution are spars .

To accurately measure even small changes in root growth, spatial resolution is of high importance. High-resolution CCD scanner images that are otherwise suited for high-throughput studies (Slovak *et al.*, 2014) won't yield the required resolution, as, even with a high scanner resolution, only ∼21 µm/pixel was achieved. Camera systems are frequently used to achieve medium resolution for root imaging and can detect subtle root growth changes (Durham Brooks, Miller and Spalding, 2010). Microscopes in conjunction with growth chambers or microfluidics chambers have been used to study root growth changes with high time resolution while inducing a stress (Grossmann *et al.*, 2011; Busch *et al.*, 2012; de Luis Balaguer *et al.*, 2016; von Wangenheim *et al.*, 2017; Stanley *et al.*, 2018). However, this method is particularly efficient to catch the extremely fast response this remains an expensive solution for tracking only ∼8 roots at a time preventing any high throughput image acquisition. Moreover, production of growth chambers, the use of confocal microscopy and dedicated software to automate these microscopes frequently pose hurdles towards their adoptability (Grossmann *et al.*, 2011; Busch *et al.*, 2012; de Luis Balaguer *et al.*, 2016; von Wangenheim *et al.*, 2017; Stanley *et al.*, 2018).

Another important element to study root growth in a high throughput manner is the ability to automatically measure the roots at different timepoints. Many efforts have been made to develop root image analysis tools that allows for this. For instance, the software MyRoot can calculate root length in a high throughput manner using scanner images (Betegón-Putze *et al.*, 2019), but requires human interaction and thus limits the processing of the time series at high time resolution. Tools allow for assessing root growth variation with high time resolution using time series images such as RootTrace and RootTip softwares (French *et al.*, 2009; Geng *et al.*, 2013) require the use of a camera which provides sufficient resolution to detect root growth variation at time-scales from 3 minutes to 15 minutes, respectively. However, the use of a camera limits high through put phenotyping e.g. from 1 for RootTrace to 6 plates for RootTip at a time containing 24 seedlings. Moreover, the downstream time series image analysis is semi-automated method which becomes very time consuming with increasing sample sizes. Lastly, a vertical confocal microscope and microfluidic system are often not provided with an automated software to calculate the root growth making hard to automate root growth analysis (Grossmann *et al.*, 2011; Busch *et al.*, 2012; de Luis Balaguer *et al.*, 2016; von Wangenheim *et al.*, 2017; Stanley *et al.*, 2018). Taken together, tools that can be used to acquire and automatically analyze root growth in a high throughput manner with high spatiotemporal resolution are currently not available.

Here, we present an analytic phenotypic platform that allows for the high throughput acquisition and quantification of early root growth response at high temporal and spatial resolution named "Root Walker". This method allows to acquire bright-field roots pictures using a microscope within minutes after imposing treatments and for up to 12 hours. The acquired images are then processed by a MATLAB® script in which roots are segmented and their growth after transfer are automatically quantified. To illustrate

the accuracy and power of this method, we used *Arabidopsis thaliana* treated with different concentrations of the auxin analog, indole-3-acetic acid (IAA), as well as another treatment with two mitogen-associated protein kinase (MAPK) inhibitors (U0126 and PD98059). We show that the Root Walker pipeline allows for the determination of root length in a high throughput manner with high time and spatial resolution. We propose that this platform is highly suited to conduct large scale targeted or exploratory quantitative genetic screens to identify genes controlling early root growth responses to stresses, nutrients or other internal or external cues.

Results

A simple growth chamber in conjunction with automated microscopy allows for root imaging at high temporal and spatial resolution

We set out to develop an automated platform for capturing root growth responses at a large-scale. For this, we wanted to image at a resolution that could capture even small changes of root growth. We also used an automated platform to capture numerous roots at a high time resolution. For this, we used an inverted BZ-X810 KEYENCE® microscope that allowed to automatically capture images with a resolution of ∼3µm/pixel for using a 2X objective (NA/0.1) or a resolution of ∼1.5 µm/pixel using a 4X objective (NA/0.2). This level of resolution allows for the detection of even subtle root growth rate changes. For capturing many roots, used an agar filled chamber in which we could place ∼20 seedlings (Figure S1a). To allow the accurate quantification of root growth responses, plants were first germinated under standard growth condition on plates and then transferred to imaging chambers containing the treatment medium (Figure S1). Per chamber, either 9 images or 17 images are acquired depending on the objective used. Up to three of these chambers can be mounted for imaging (Figure S1b-c), resulting in an imaging capacity of ∼60 seedlings per experimental round. As we used 4 microscopes, we were able to measure ∼240 roots at a time. The described imaging setup allows for taking images at a highly frequent rate which varies according to the objective used and the number of imaging chambers loaded on the microscope stage. For example, these values are ranging from 18 seconds loading one chamber using the 2X objective to 59s loading 3 chambers with the 4X objective. Here, we used two different setups, acquiring images every minute for 60 minutes with the 4X objective and every 5 minutes for 12 hours with the 2X objectives. Taken together, this microscope set up provides a platform to acquire images of roots at high time and spatial resolution in a high-throughput manner.

A user-friendly software-tool allows to calculate the root length in an automated and high-throughput manner

After successful image acquisition, each image is processed by a user-friendly MATLAB® script that only requires three user inputs: i) select a parent folder containing the images; ii) select a folder to store the output files, and iii) supply a descriptive file-prefix to be used for the output files. This script automatically quantifies root length in the time series images acquired with the Keyence® BZ-X810 microscope of

Arabidopsis thaliana roots by performing several steps: (1) convert raw images to a large stitched image (2) transform into a binarized stitched image, (3) convert binary stitched images into arrays of root center midpoints, (4) "walk" along the center root array to virtually reconstruct the root, (5) calculate root length and remove outliers, (6) allow for quality control (QC) through the generation of videos and graphical plot output files (7) export of raw data in .csv files (8) further data analysis and graphs can be continued using Excel® (Figure 1a). The script takes only a ∼190 ms per single image (if 9 images is contained in one stitched image the time is ∼1.710 seconds per stitches) using a desktop computer with Intel® Xeon® W-2135 CPU @3.70 GHz and 64GB of random-access memory. Note that we developed two different scripts adjusted to quantify root growth when acquiring images every minute for 60 minutes using the 4X objectives and every 5 minutes for 12 hours using the 2X objective as mentioned in the previous paragraph. In the subsequent sections, we describe the steps of the software in detail.

Root segmentation

The first step (1) of the algorithm consists of stitching all images that were acquired during a single time point together (Figure 1b). The next step (2) is then to accurately segment all roots that are contained in the stitched image enabling a precise measurement of the root length (Figure 1c). For this, a binarized image is generated using Otsu's thresholding method, which minimizes the intraclass variance of the binary pixels (Figure 1c). Then a locally adaptative thresholding, and darker foreground than background methods are applied to increase the thresholding accuracy (Figure 1c). Finally, background noise and air bubbles coming from the camera sensor itself or from the plant transfer procedure to the imaging chamber are eliminated, respectively. This step removes small objects (< 8000 pixels) and very large objects (> 150 000 pixels) to obtain images with only roots as the remaining objects (Figure 1c). Note that we particularly focused on annotating carefully the MATLAB® script to offer the possibility for the users to fine tune these parameters depending on the users' needs and deliver a versatile tool. The resulting image contains only segmented roots. However, these segmented roots have very jagged, fractal-like edges, which when used to track the center line of each root leads to an overestimation of the root length (analogous to the coastline paradox). To reduce this error, the image is convolved with a smoothing kernel to smooth out the jagged root edges. The borders are then cleared of any black pixels created during the smoothing process (Figure 1c). The binarized stitched images are now saved for the subsequent generation of diagnostic videos and data analysis.

Determination of the root length using the Root Walker

Once, the images are segmented, the root center line is determined based on the center array of each root object to calculate the root length at each time point (step 3, Figure 1d). Each stitched image is then processed to create a set of arrays that corresponds to the center point of each root for each row of every image. This process consists of several distinct steps: (1) for each row of each stitched image, the indices of the black pixels (Figure 1d), corresponding to an object are recorded. This set of indices is saved as a vector for each row of each stitched image and is of the same height in dimension as the image (Figure 6a, eg. 1920 pixels). (2) The entire set of black pixel indices is separated into vectors of connected sets of black pixel indices, separating each object that is not touching or connected in the image. The objects are

now considered as distinct which then allows to process them individually in the next steps and iterative functions. (3) The mean of each vector of the black pixel indices is taken, replacing the vector with a single value corresponding to the center point index for each object for each row in the stitched image. As a result, the data set is the same height as the input stitched image but is now much smaller in width which reduces the amount of data to process and speeds up the analysis (Figure 1e). This step is performed for each row of each stitched image that was previously created.

The center point index array does not reflect the root length after transfer yet as each root object is stored in a data set which is the same height but for which the width is variable as indicated in Figure 1e. Therefore, further processing needs to be conducted by "walking" along each root pixel array previously generated to artificially reconstruct the root (step 4, Figure 1f). The value of the center point index array is used to determine which objects correspond to roots based on its horizontal distance in the next row. The method selects the first center point index array as a start and loops through each row of the array, stepping down each row from the top to the bottom, and determines if there is an index in the next row that is within a certain horizontal distance (default of 30 for the 60 minutes timelapse script or 20 pixels for 12 hours timelapse script) of the root's center point in the previous row. Note that we particularly focused on annotating carefully the MATLAB® script to offer the possibility for the users to fine tune these parameters depending on the users' needs and deliver a versatile tool. This process is repeated for the entire center index array, saving each center point within that set criteria as the next value in that "root" vector (Figure 1f). The method repeats this process for each timestep, for each stitched image, for each starting point or object in the center point index array, and for each row of the stitched image. While this is a repetitive process, it is computationally extremely fast due to the simplicity of the calculation being performed. After the method has carried out this step, the dataset now includes position vectors for each center point for each row of each object in each stitched image.

To increase the robustness of our root growth rate measurements, the software next integrates different timesteps and conducts further processing. This aims to address curvature due to circumnutation (Taylor *et al.*, 2021) that may create imprecision in measuring the root growth, as well as potential distortions due to our focus on pixel root center array (we need three width pixels but a thresholded root tip may contain only one or two pixels in some timesteps). To overcome these issues, only new growth is being measured at each time point and this is achieved by overwriting each timestep with the previous timestep ensuring that only new growth relative to the previous root tip location is measured.

Next, the position vectors for each root are utilized to perform a center line distance calculation to determine the length of each root at each timestep (Figure 1g and Figure S2). The center line positions for each row are used to calculate the distance between each row, summing each small change in length between each row of the image to calculate the entire root length. This process is completed for all roots in the current root center array.

Outlier removal

The method then filters out outlier growth rates that might correspond to image processing errors or the failure to remove a non-root object from analysis earlier in the method (step 5, Figure 1h). This method utilizes the root length data that was previously generated and removes any elements that do not change in length for 20 or 45 timesteps, for short or long-time lapses, respectively. Note that we particularly

203 focused on annotating carefully the MATLAB® script to offer the possibility for the users to fine tune these
204 parameters depending on the users' needs and deliver a versatile. These outliers might be roots that are
205 not growing due to damage while transferring them to the imaging chamber referenced as "stuck" roots
206 or a non-root object (such as a scratch or a bubble) that was included in the binarized image and remains
207 in the same location. The method also removes any roots that "jump", having an increase in length greater
208 than 45 pixels in a one timestep for our long time-lapse set up and 20 pixels for the short time-lapse set
209 up representing approximately in both cases a jump of ~28µm per minute, being more than 7 times faster
210 than the root growth rate that we observe in healthy roots (~3.9µm/min, Figure 1h). Note that we
211 particularly focused on annotating carefully the MATLAB® script to offer the possibility for the users to
212 fine tune these parameters depending on the users' needs and deliver a versatile. Depending on the
213 experimental setup, the percentage of "stuck" and 'jump" events detected, as well as undetected, false
214 negatives led to a loss of about 8% for the 60 minutes script (124 roots detected and 114 roots for which
215 the root length after transfer has been calculated over 7 independent experiments) and about 25% for 12
216 hours script (171 roots detected and 129 roots for which the root length after transfer has been
217 determined over 6 independent experiments) in our experimental set-up. Note that we did not detect any
218 false positives in this set up. After outliers and artifacts removal, the root length for each timestep is used
219 to determine the amount of new growth of each root per timestep by subtracting the previous timestep's
220 length from the current timestep as previously described. This is performed iteratively for each timestep
221 to construct a dataset containing the change in root length for each root in each timestep.
222
223 **Generation of output files**
224
225 To allow for a quality control step of the analysis, a timelapse video with annotations for manual
226 inspection is generated (step 6, Figure 1i and Video S1). For this, the raw and processed stitched images
227 are displayed as a video with the calculated root center lines plotted on the associated figure (Video S1).
228 The video includes the raw image with center lines for all detected roots, including "Jump" and "Stuck"
229 roots, as well as the binarized and thresholded image that contains the root objects that are remaining
230 after the artifacts and outliers removal. This step takes approximately half of the full image analysis time
231 (~95 ms per single image (if 9 images is contained in one stitched image the time is 855ms per stitches)
232 using a processor Intel® Xeon® W-2135 CPU @3.70 GHz and 64GB of random-access memory. If diagnostic
233 videos are not needed, we provided an alternative script – thus, one script including this step and one in
234 which this step is omitted.
235 To provide a succinct analysis of the experiment, the dataset is plotted for visual inspection (step6) by
236 generating two plots. The first plot contains the root lengths versus time, showing each individual root
237 throughout the entire experiment. The second plot groups the roots by genotype and condition and plots
238 the average root lengths for each group versus time. Both plots are saved and exported as .jpeg. Note that
239 these plots are being intended for visual inspection and can be used to detect potential outliers that were
240 not detected by the automated analysis or to help to adapt in a fast manner every tunable parameters in
241 the script.
242 The processed root datasets are exported as .csv (using pixels as units) to allow for a comprehensive data
243 analysis (step 7, Figure 1j). To facilitate high throughput data organization in the .csv output file, the date,
244 the number of the replicate, the genotype and the growing conditions are directly extracted from the

245 parent folder. The data organization is made to be compatible with the "Pivot Table" function in Excel®
246 allowing to easily process large amounts of data (Figure 1j). Using this Excel® function the remaining
247 outliers, which might have passed the previous thresholding steps to filter out objects that "Jump" and
248 are "Stuck" can be removed. Moreover, the pixels units can be converted into physical measurements and
249 any root length derived traits, such as root growth rate and other parameters can be calculated (step 8).
250
251 **Validation of the platform studying the early root growth response to the auxin analog indole-3-acetic**
252 **acid (IAA) for 20 minutes**
253
254 Before submitting roots to a treatment condition, we evaluated the accuracy of our method by comparing
255 root growth data measured by a human observer versus the root walker. This experiment revealed that
256 our tool is highly accurate since no significant differences were observed when comparing the
257 quantification methods (Figure 2a-d). Moreover, scatter plot with linear regression and Pearson
258 correlation matrix analysis based on the root growth rate confirm our finding further validating the
259 reliability of our quantification tool (Figure 1e-f). The root growth rate in our system was ~2.3 +/-0.52
260 µm/min thus being in the same range as previously reported (Figure 2; Serre et al., 2021 Nat Plants;
261 Fendrych et al., 2018 Nat Plants, Prigge et al., 2020, eLife). To test the utility of the Root Walker platform,
262 we studied the response of Arabidopsis root growth rate upon treatment with indole-3-acetic acid (IAA).
263 To our knowledge this is the only treatment which has been reported to impact the root growth within
264 minutes when applied in nanomolar range (Serre et al., 2021 Nat Plants; Fendrych et al., 2018 Nat Plants,
265 Prigge et al., 2020, eLife). We applied IAA at 1nM (IAA[1]), 10nM (IAA[10]) and 100nM (IAA[100]) and
266 followed the root growth taking images every minute for an hour. In standard condition, the root growth
267 rate was still in the range of our previous results ~3.9+/-1.37 µm/min (Figure 3). Furthermore, in line with
268 the literature, we observed a decrease of the root growth rate in a concentration dependent manner in
269 the order of µm per minute (Figure 3 and Video S2, Serre et al. 2021). A significant decrease of the root
270 length was already observed 1 minute after transfer upon treatment with 10nM IAA and 100nM IAA
271 (Figure 3b). At the lower concentration of 1nM IAA, the first significant difference of root growth rate was
272 observed after 11 minutes timepoint, highlighting a concentration-dependent root growth response
273 (Figure 3b). Altogether, these results show that the Root Walker platform can capture extremely fast root
274 growth changes through its capability to acquire images with high time and spatial resolution and with
275 high throughput, making it a powerful tool for studying root growth responses.
276
277 **Investigation of two MAPK inhibitors on the root growth for 12 hours**
278
279 As we had shown that our platform is very well suited to study very fast responses as observed for IAA,
280 we also wanted to test whether it was capable to accurately capture growth responses that only occur
281 after several hours. For this, we investigated the impact of two well-known mitogen associated protein
282 kinase homolog 2 (MPK2) inhibitors on root growth. The ubiquitous MPK2 is part of the MAPK
283 phosphorylation cascade which is central in the regulation of eukaryotic developmental signaling events
284 (Ge, Fu and Meadows, 2002; Hotokezaka *et al.*, 2002; Bjornson *et al.*, 2014). We used two inhibitors of
285 MPK2 that have different modes of action: PD98059 inhibits the MAPK cascade by binding the inactive
286 form of MPK2 while U0126 directly inhibits MPK2 kinase activity (Bjornson *et al.*, 2014). To study the root

growth response to these MPK2 inhibitors, we monitored root length for 12 hours taking images every 5 minutes. We noticed that the root growth rate (mm/hour) was significantly lower when plants were exposed to U0126, but no differences were apparent for PD98059 compared to the mock treatment (Figure 4 Video S3). Moreover, a statistical different root length between U0126 and mock conditions was already apparent after 2 hour and 25 minutes (Figure 4b). We concluded that the inhibition of MPK2 kinase activity rather than the sequestration of the inactive form is critical in regulating root growth. This experiment showed that the Root Walker platform can shed light on new early root growth regulatory mechanisms.

DISCUSSION

Here, we have described a new analytic high-throughput platform with high spatial and temporal resolution allowing to accurately quantify early root growth responses to different external stimuli. Minutes after being transferred to imaging chambers containing the treatment of about 20 roots per imaging chamber can be imaged at the same time. By using an automated digital microscope, we were able to mount 3 chambers per microscope and by using 4 microscopes in parallel, resulting in 240 roots being imaged at a time. Using such a system, a time resolution of more than 30 seconds after the transfer could be achieved at a spatial resolution of ~3µm/pixel for 2X objective and ~1.5 µm/pixel for 4X objective. To process the data, we developed a MATLAB® pipeline to automatically quantify the root lengths from these experiments. This is step is particularly user friendly since the initialization required only three user inputs and works without any image preprocessing or human intervention. The platform presented here is highly versatile and can be then adoptable by a broader set of scientist; 1) the Keyence® microscope is affordable compared to confocal microscopes, 2) the imaging chambers used are commercially available and can be used on any microscope types, 3) the script is tediously annotated offering to the user to fine tune several parameters (thresholding value, outliers object size, stitching overlap, distance of the index, stuck and jump) without requiring any skills in script coding, 4) the script can work on any type of stitched images, 5) the root growth tracking time is wide, ranging from minutes to 12 hours.

To demonstrate the utility and the power of this approach to capture early root growth responses, we utilized the exogenous application of IAA for which, the root growth has been described to be inhibited minutes after being exposed to this hormone at nanomolar ranges. Using our platform, we observed that this response was concentration-dependent and occurred minutes after transfer confirming the sensitivity of the Root Walker platform. To show the versatility of the platform at a different timescale, we investigated longer root growth response, 12 hours after transfer using two MAPK inhibitors known to interfere with the MAPK signaling cascade. This revealed that only U0126 triggers a significant root growth decrease, suggesting that MPK2 kinase activity is required to regulate root growth. In the literature, discrepancy between these inhibitors has been already reported while studying the plant general stress response in shoots (Bjornson *et al.*, 2014). They found that the MAPK signaling cascade is critical in mediating the rapid stress response element through the CALMODULIN-BINDING TRANSCRIPTIONAL ACTIVATOR 3 (Bjornson *et al.*, 2014). However, opposite to our findings, in shoots, only PD98059 was able to delay the response while no changes were observed in presence of U0126 highlighting that the sequestration of MPK2 rather than its catalytic activity is critical in triggering this

329 rapid response in shoots. Taken together, this might suggest that there are tissue and time scale
330 dependent MPK2 regulatory mechanisms in plants.
331 To conclude, the Root Walker platform is an excellent tool to study early root growth responses ranging
332 from minutes to 12 hours after transfer to the treatment conditions. Compared to other publicly available
333 platforms or software, the Root Walker provides a simple but comprehensive all-in-1 large-scale pipeline
334 to study early root growth rate (Slovak *et al.*, 2014; Durham Brooks, Miller and Spalding, 2010; Betegón-
335 Putze *et al.*, 2019; French *et al.*, 2009; Geng *et al.*, 2013; von Wangenheim *et al.*, 2017). It not only allows
336 to acquire images with high spatiotemporal resolution in a high throughput manner but also to analyze
337 root growth automatically. We do think that this comprehensive platform is a prime choice to conduct
338 large scale screening or early root growth response to various stimuli which might enable the
339 identification of genes involved in sensing external stimuli.
340
341 **Experimental procedures**
342
343 **Plant materials and growth conditions.** For surface sterilization, *Arabidopsis thaliana* seeds
344 that had been produced under uniform growth conditions and were placed for 1 h in opened 1.5-
345 mL Eppendorf tubes in a sealed box containing chlorine gas generated from 130 mL of 10%
346 sodium hypochlorite and 3.5 mL of 37% hydrochloric acid. For stratification, seeds were imbibed
347 in water and stratified in the dark at 4 °C for 2-3 days. Seeds were then put on the surface of
348 media described in Gruber et al., 2013, using 12-cm x 12-cm square plates (Gruber *et al.*, 2013).
349 The Gruber et al., 2013 media contains, 750 µM of $MgSO_4$-7H2O, 625 µM of KH_2PO_4, 1000 µM
350 of NH_4NO_3, 9400 µM of KNO_3, 1500 µM of $CaCL_2$-$2H_2O$, 0.055 µM of $CoCL_2$-$6H_2O$, 0.053 µM of
351 $CuCl_2$-$2H_2O$, 50 µM of H_3BO_3, 2.5 µM of KI, 50 µM of $MnCl_2$-$4H_2O$, 0.52 µM of Na_2MoO_4-$2H_2O$,
352 15 µM of $ZnCl_2$, 75 µM of Na-Fe-EDTA, 1000 µM of MES adjusted to pH 5.5 with KOH and 0.5%
353 sucrose and 1% BactoAgar®. Plants were grown in long day conditions (16/8h) in walk in growth
354 chambers at 21°C, 50uM light intensity, 60% humidity. During nighttime, temperature was
355 decreased to 15°C.
356
357 **Phenotyping of the root growth responses.** Wild type seeds were sowed in media described
358 in Gruber et al., 2013 and stratified for 2-3 days at 4°C (Gruber *et al.*, 2013). Five days after
359 planting, about 20 seedlings were transferred using forceps to an imaging chamber (Lab-Tek,
360 Chambers #1.0 Borosilicate Coverglass System, catalog number: 155361) filled with medium
361 described in Gruber et al., 2013. Note that the transfer took about 45-60 seconds. Images were
362 acquired every minute or 5 minutes for 1 hours or 12 hours, respectively, in brightfield conditions
363 using a Keyence® microscope model BZ-X810 with a BZ NIKON Objective Lens (4X or 2X) CFI
364 Plan-Apo Lambda.
365
366 **Treatment with IAA, U0126 and PD98059.** The imaging chamber was filled up with the media
367 described in Gruber et al., 2013 in which IAA dissolved in DMSO (stock solution 1000X compared
368 to the final solution) at 1nM, 10nM or 100nM and DMSO was added (Gruber *et al.*, 2013).
369 Moreover, U0126 and PD98059 dissolved in DMSO (stock solution 20mM or 10mM, respectively)

370 at a concentration of 10μM and DMSO were added to the gruber media when poured to the
371 imaging chamber
372
373 **Manual measurement of the root growth.** Time lapse images were used to create videos with
374 the Keyence software®. The videos were opened in Fiji (Schindelin *et al.*, 2012) and the root tip
375 displacement was measured using the segmented line tool at each time point.
376
377 **Statistical analysis.** Each experiment has been repeated independently at least twice, as in
378 every case the same trend has been recorded for independent experiments, the data have been
379 pooled for further statistical analysis. Each sample were subjected to four different normality tests
380 (Jarque-Bera, Lilliefors, Anderson-Darling and Shapiro-Wilk), sample were considered as a
381 Gaussian distribution when at least one test was significant ($p<0.05$) using Xlstat. As a normal
382 distribution was observed a two-ways ANOVA coupled with post hoc Tukey test was performed
383 ($p<0.05$) using Xlstat. As a normal distribution was not observed at two-ways Kruskal-Wallis
384 coupled with post hoc Steel-Dwass-Critchlow-Fligner procedure was performed ($p<0.05$) using
385 Xlstat. The type of test performed in indicated in the figure legend.
386
387 **Acknowledgements:** We thank all the Busch lab members for critical discussions. This study was funded
388 by the National Institute of General Medical Sciences of the National Institutes of Health (grant number
389 R01GM127759 to W. Busch), and start-up funds from the Salk Institute for Biological Studies (W. Busch).
390 M.P. Platre was supported by a long-term postdoctoral fellowship (LT000340/2019 L) by the Human
391 Frontier Science Program Organization.
392
393 **Declaration of interest:** The authors declare no conflict of interest.

394 **Code availability:** Matlab® script can be found here, https://github.com/mplatre/Root-Walker-Script.git

395 REFERENCES
396
397 Betegón-Putze, I. *et al.* (2019) 'MyROOT: a method and software for the semiautomatic measurement of
398 primary root length in Arabidopsis seedlings', *The Plant Journal*, 98(6), pp. 1145–1156. Available at:
399 https://doi.org/10.1111/tpj.14297.

400 Bjornson, M. *et al.* (2014) 'Distinct Roles for Mitogen-Activated Protein Kinase Signaling and
401 CALMODULIN-BINDING TRANSCRIPTIONAL ACTIVATOR3 in Regulating the Peak Time and Amplitude of
402 the Plant General Stress Response1[W][OPEN]', *Plant Physiology*, 166(2), pp. 988–996. Available at:
403 https://doi.org/10.1104/pp.114.245944.

404 Busch, W. *et al.* (2012) 'A microfluidic device and computational platform for high-throughput live imaging
405 of gene expression', *Nature Methods*, 9(11), pp. 1101–1106. Available at:
406 https://doi.org/10.1038/nmeth.2185.

407 Durham Brooks, T.L., Miller, N.D. and Spalding, E.P. (2010) 'Plasticity of Arabidopsis Root Gravitropism
408 throughout a Multidimensional Condition Space Quantified by Automated Image Analysis', *Plant
409 Physiology*, 152(1), pp. 206–216. Available at: https://doi.org/10.1104/pp.109.145292.

410 French, A. *et al.* (2009) 'High-Throughput Quantification of Root Growth Using a Novel Image-Analysis
411 Tool', *Plant Physiology*, 150(4), pp. 1784–1795. Available at: https://doi.org/10.1104/pp.109.140558.

412 Ge, X., Fu, Y.M. and Meadows, G.G. (2002) 'U0126, a mitogen-activated protein kinase kinase inhibitor,
413 inhibits the invasion of human A375 melanoma cells', *Cancer Letters*, 179(2), pp. 133–140. Available at:
414 https://doi.org/10.1016/s0304-3835(02)00004-6.

415 Geng, Y. *et al.* (2013) 'A Spatio-Temporal Understanding of Growth Regulation during the Salt Stress
416 Response in Arabidopsis', *The Plant Cell*, 25(6), pp. 2132–2154. Available at:
417 https://doi.org/10.1105/tpc.113.112896.

418 Grossmann, G. *et al.* (2011) 'The RootChip: An Integrated Microfluidic Chip for Plant Science', *THE PLANT*
419 *CELL ONLINE*, 23(12), pp. 4234–4240. Available at: https://doi.org/10.1105/tpc.111.092577.

420 Gruber, B.D. *et al.* (2013) 'Plasticity of the Arabidopsis Root System under Nutrient Deficiencies', *Plant*
421 *Physiology*, 163(1), pp. 161–179. Available at: https://doi.org/10.1104/pp.113.218453.

422 Hotokezaka, H. *et al.* (2002) 'U0126 and PD98059, specific inhibitors of MEK, accelerate differentiation of
423 RAW264.7 cells into osteoclast-like cells', *The Journal of Biological Chemistry*, 277(49), pp. 47366–47372.
424 Available at: https://doi.org/10.1074/jbc.M208284200.

425 Jia, Z., Giehl, R.F.H. and von Wirén, N. (2022) 'Nutrient–hormone relations: Driving root plasticity in
426 plants', *Molecular Plant*, 15(1), pp. 86–103. Available at: https://doi.org/10.1016/j.molp.2021.12.004.

427 Li, B. *et al.* (2019) 'GSNOR provides plant tolerance to iron toxicity via preventing iron-dependent
428 nitrosative and oxidative cytotoxicity', *Nature Communications*, 10, p. 13.

429 de Luis Balaguer, M.A. *et al.* (2016) 'Multi-sample Arabidopsis Growth and Imaging Chamber (MAGIC) for
430 long term imaging in the ZEISS Lightsheet Z.1', *Developmental Biology*, 419(1), pp. 19–25. Available at:
431 https://doi.org/10.1016/j.ydbio.2016.05.029.

432 Morris, E.C. *et al.* (2017) 'Shaping 3D Root System Architecture', *Current Biology*, 27(17), pp. R919–R930.
433 Available at: https://doi.org/10.1016/j.cub.2017.06.043.

434 Platre, M.P. *et al.* (2022) 'The receptor kinase SRF3 coordinates iron-level and flagellin dependent defense
435 and growth responses in plants', *Nature Communications*, 13(1), p. 4445. Available at:
436 https://doi.org/10.1038/s41467-022-32167-6.

437 Satbhai, S.B. *et al.* (2017) 'Natural allelic variation of FRO2 modulates Arabidopsis root growth under iron
438 deficiency', *Nature Communications*, 8, p. 15603. Available at: https://doi.org/10.1038/ncomms15603.

439 Schindelin, J. *et al.* (2012) 'Fiji: an open-source platform for biological-image analysis', *Nature Methods*,
440 9(7), pp. 676–682. Available at: https://doi.org/10.1038/nmeth.2019.

441 Slovak, R. *et al.* (2014) 'A Scalable Open-Source Pipeline for Large-Scale Root Phenotyping of Arabidopsis',
442 *The Plant Cell*, 26(6), pp. 2390–2403. Available at: https://doi.org/10.1105/tpc.114.124032.

443 Stanley, C.E. *et al.* (2018) 'Dual-flow-RootChip reveals local adaptations of roots towards environmental
444 asymmetry at the physiological and genetic levels', *The New Phytologist*, 217(3), pp. 1357–1369. Available
445 at: https://doi.org/10.1111/nph.14887.

446 Taylor, I. *et al.* (2021) 'Mechanism and function of root circumnutation', *Proceedings of the National*
447 *Academy of Sciences*, 118(8), p. e2018940118. Available at: https://doi.org/10.1073/pnas.2018940118.

448 von Wangenheim, D. *et al.* (2017) 'Live tracking of moving samples in confocal microscopy for vertically
449 grown roots', *eLife*. Edited by C.S. Hardtke, 6, p. e26792. Available at:
450 https://doi.org/10.7554/eLife.26792.

451

a

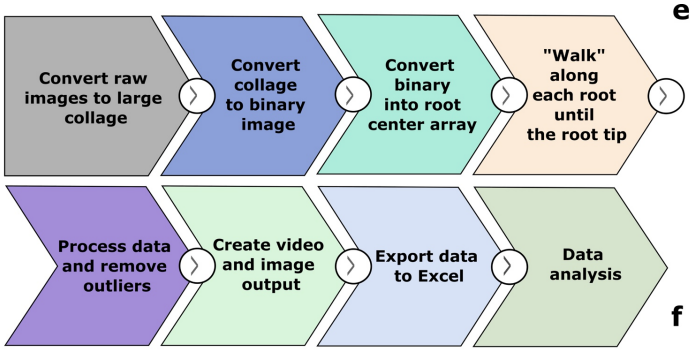

b

Image acquisition

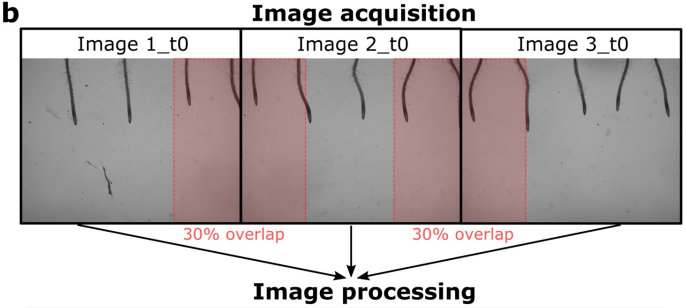

Image processing

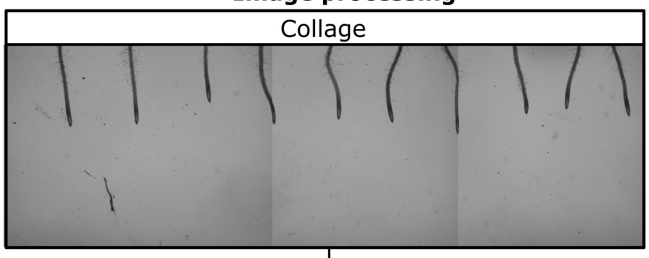

c

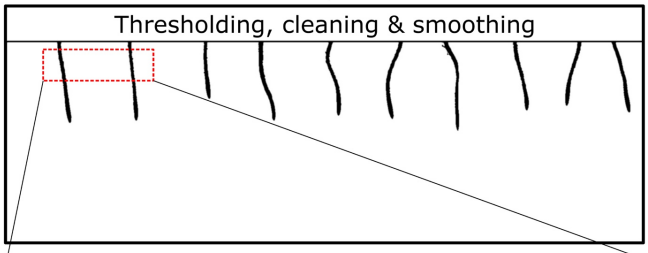

Image matrix

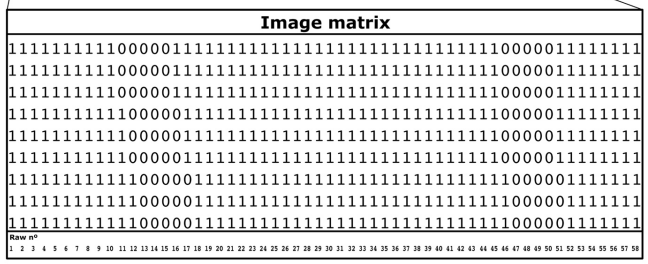

d

Determining root center array

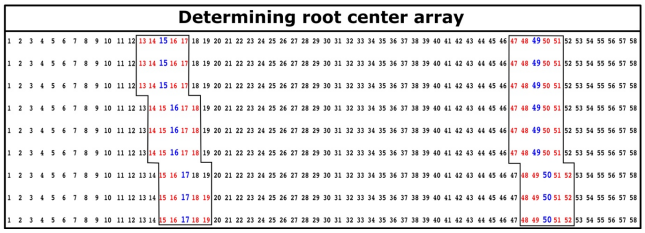

e

Row	Walk along the root
1	130 480 640 860 990 1300 1440 1505
2	130 480 640 860 990 1300 1440 1560
3	130 480 640 860 990 1300 1440 1560
4	130 480 641 860 990 1299 1440 1564
5	132 480 642 860 990 1298 1440 1565
6	133 480 642 860 990 1297 1440 1568
7	133 481 860 991 1297 1440 1564
8	135 481 860 992 1298 1440 1564
9	135 481 860 993 1299 1440

f

Row	Reconstructing the root
1	130 480 640 860 990 1300 1440 1505
2	130 480 640 860 990 1300 1440 1560
3	130 480 640 860 990 1300 1440 1560
4	130 480 641 860 990 1299 1440 1564
5	132 480 642 860 990 1298 1440 1565
6	133 480 642 860 990 1297 1440 1568
7	133 481 860 991 1297 1440 1564
8	135 481 860 992 1298 1440 1564
9	135 481 860 993 1299 1440

g

Row	Calculating distance
1	(130) (480) (...) (...) (...) (...) (...)
	↓1 ↓1
2	(130) (480)
	↓1 ↓1
3	(130) (480)
	↓1 ↓1
4	(130) (480)
	↓2.32 ↓1
5	(132) (480)

h

Removing outliers

1) Roots that grow faster than "X" pixels per time point "jump"

2) Root that do not grow during 'n' time points "stuck"

i

Output files generation

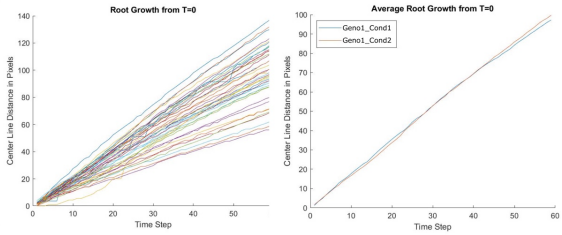

j

	A	B	C	D	E	F	G
1	DATE	EXP	Genotype	Condition	Root_number	Timestep_min	Root length (pixel)
2	YYYYMMDD	EXP_X	Geno1	Cond1	1	1	0
3	YYYYMMDD	EXP_X	Geno1	Cond1	1	2	1.55783
4	YYYYMMDD	EXP_X	Geno1	Cond1	1	3	1.97253
5	YYYYMMDD	EXP_X	Geno1	Cond1	1	4	2.59321
6	YYYYMMDD	EXP_X	Geno1	Cond1	1	5	3.14682
7	YYYYMMDD	EXP_X	Geno1	Cond1	1	6	3.47865
8	YYYYMMDD	EXP_X	Geno1	Cond1	1	7	4.07276
9	YYYYMMDD	EXP_X	Geno1	Cond1	1	8	4.43287
10	YYYYMMDD	EXP_X	Geno1	Cond1	1	9	5.24783
11	YYYYMMDD	EXP_X	Geno1	Cond1	1	10	5.99938

Figure 1. Overview of the Root Walker analysis platform. (a) Step diagram of the root walker analysis platform. b) Pictures that are acquired overlap by 30% . (**b**) Stitched picture (collage). (**c**) Upper panel, binary image obtained by using three steps: thresholding, removing background and smoothing. Lower panel, binary matrix (subset from red box) obtained from binary image, 0 represents a black pixel and 1 a white pixel. (**d**) Determination of the Root Center Array from the binary image using connected sets of black pixels and extraction of the root center values (blue text). (**e**) Root center value array stored as a data sheet. The algorithm walks down each row in the matrix to determine if there is a connected object in the next row progressing vertically down the image. The connected objects are represented by the same color and the number represent the root center array value. (**f**) The connected objects are stored separately as arrays in a data sheet. (**g**) Distances are then calculated for each root array in the matrix to calculate the root length. (**h**) removal of improbable root growth values. (**i**) Graphical output file representing the root length (in pixels) of each root, left, or in for the same genotype in one condition according to time. (**j**) Example of the data stored in the .csv file when opened in Excel®.

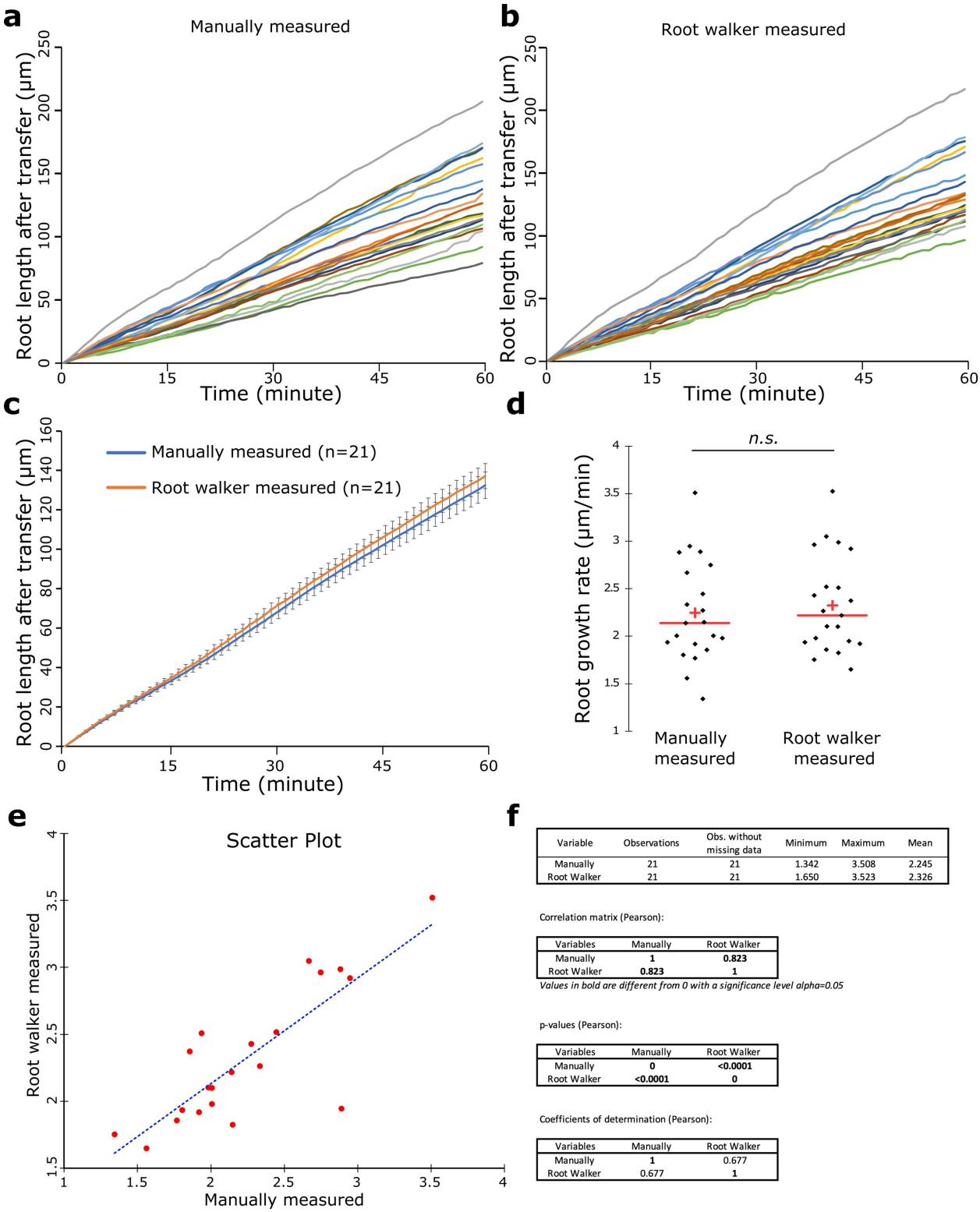

f

Variable	Observations	Obs. without missing data	Minimum	Maximum	Mean
Manually	21	21	1.342	3.508	2.245
Root Walker	21	21	1.650	3.523	2.326

Correlation matrix (Pearson):

Variables	Manually	Root Walker
Manually	**1**	**0.823**
Root Walker	**0.823**	**1**

Values in bold are different from 0 with a significance level alpha=0.05

p-values (Pearson):

Variables	Manually	Root Walker
Manually	**0**	**<0.0001**
Root Walker	**<0.0001**	**0**

Coefficients of determination (Pearson):

Variables	Manually	Root Walker
Manually	**1**	0.677
Root Walker	0.677	**1**

Figure 2. Comparison of root growth rate between Root Walker analysis script and human observer. (**a-c**) Root growth of individual 7-day old seedlings after transfer to the imaging chamber containing standard medium. Root length increase of individual roots over 60 minutes manually quantified (**a**), by the Root Walker script (**b**), or averaged (**c**). Error bars represent the standard deviation. (**d**) Root growth rate of data presented in a,b. [two-way student t-test; ($p<0.05$)]. n.s., non-significant. Red crosses represent the average and the red bars the median. Black dots individual measurements. (**e**) Scatter plot of the manually measured values in function of the root walker measured values. (**f**) From top to bottom, descriptive data of the root growth rate values manually measured, or root walker measured, correlation matric (Pearson), p-values (Pearson) and coefficient of determination (Pearson).

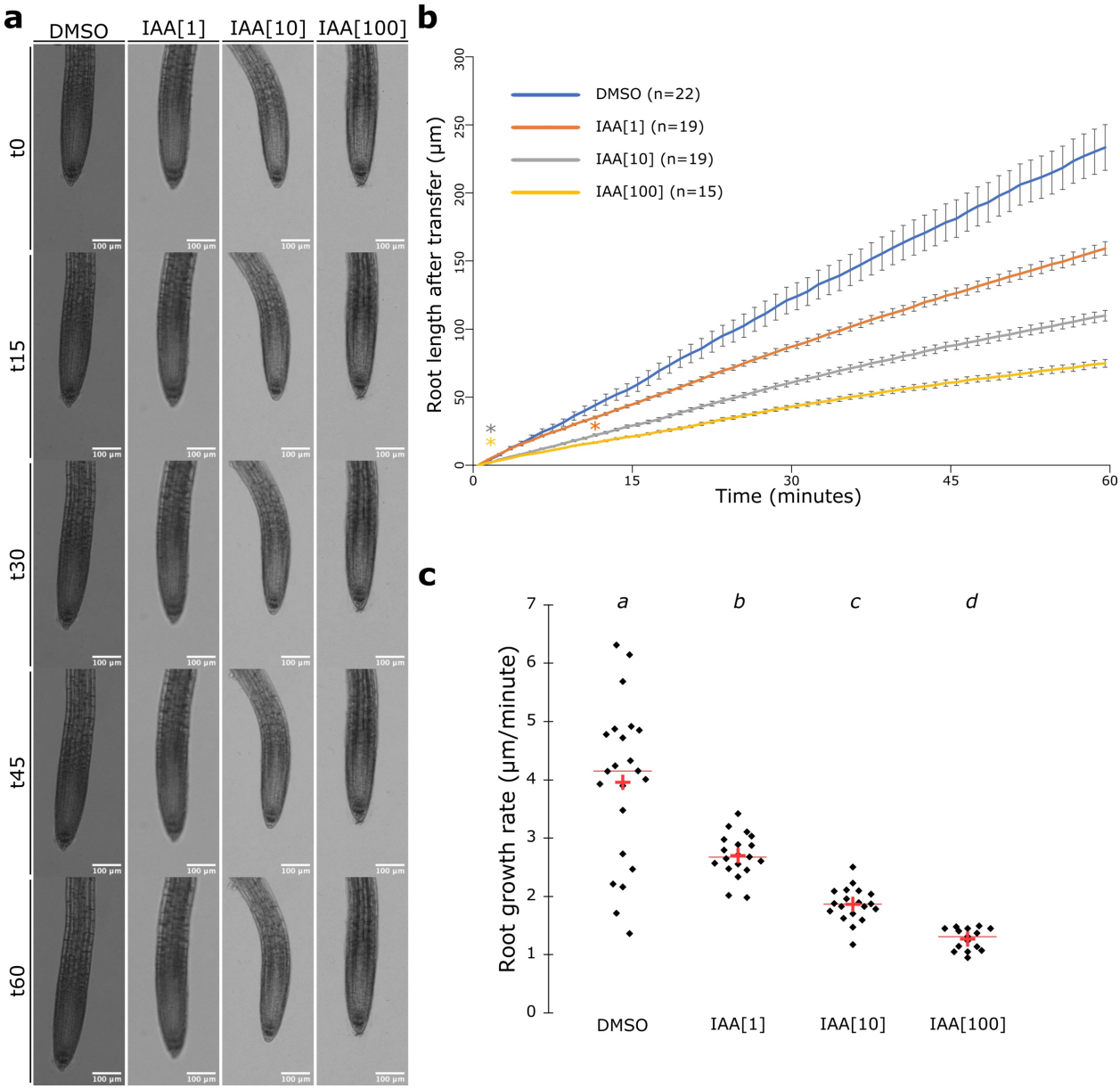

Figure 3. Exogenous application of Indole-3-acetic acid for an hour restricts root growth in a concentration-dependent manner. (**a**) From left to right, representative images of roots of 5-day old seedlings treated with DMSO, IAA at 1nM, 10nM and 100nM for over the course of one hour. Scale bar, 100 µm. (**b**) Graphical representation of the root length increases over time after transfer to treatment medium. [two-way student t-test; ($p<0.05$)]. Asterisks indicate statistical differences compared to the DMSO and the color corresponds to the curve. Error bars represent the standard deviation. (**c**) Quantification of root growth rate expressed in µm per minute of seedlings treated with DMSO, IAA at 1nM, 10nM and 100nM for an hour. [two-way ANOVA followed by a Fisher LSD test; letters indicate statistical differences ($p<0.05$)]. Red crosses represent the average and the red bars the median. Black dots individual measurements

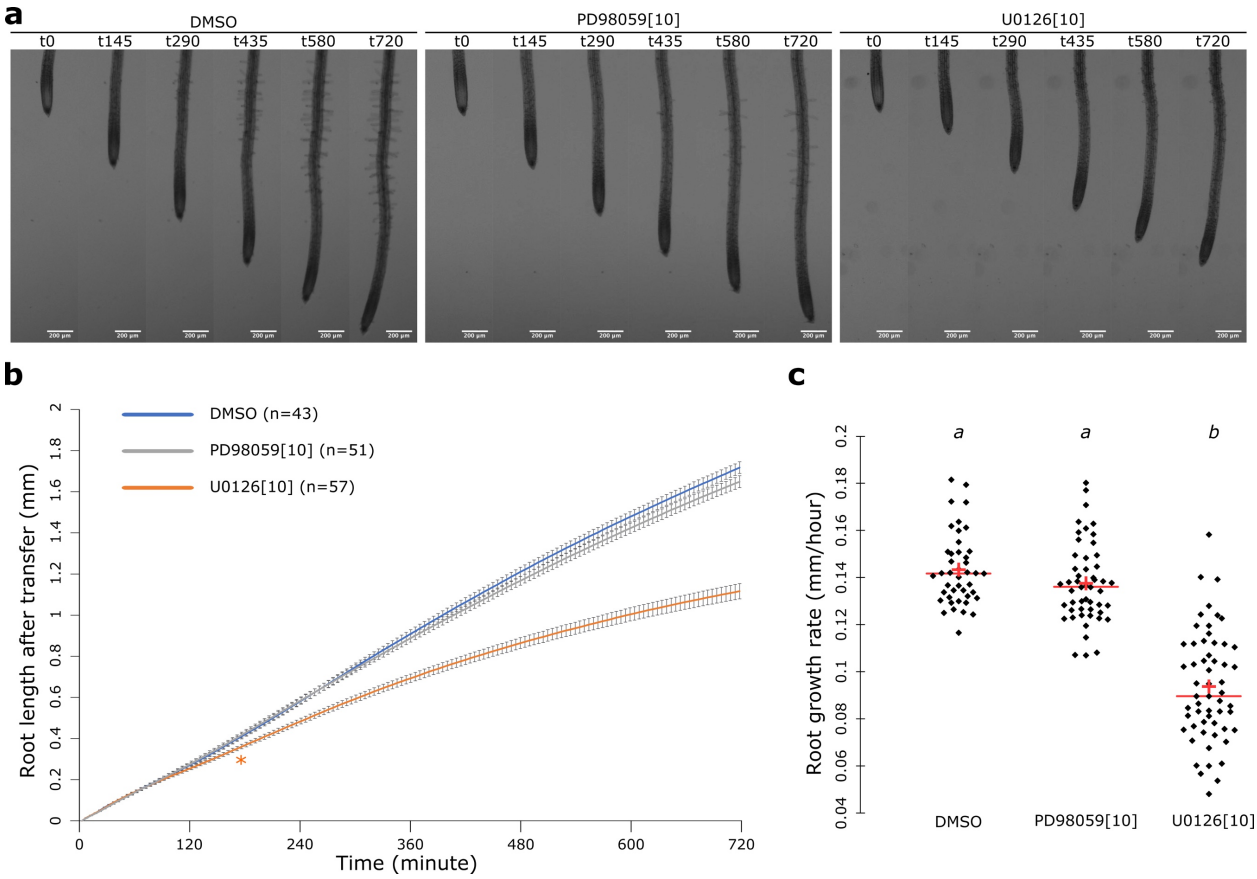

Figure 4. Exogenous application of the MPK cascade inhibitor U0126 but not PD98059 restricts root growth. (**a**) From left to right, representative images of roots of 5-day old seedlings treated with DMSO, PD98059 and U0126 at 10µM over the course of 12 hours. Scale bar, 200 µm. (**b**) Graphical representation of the root length increases after transfer to DMSO, PD98059 and U0126 at 10µM for 12 hours. [two-way student t-test; ($p<0.05$)]. Asterisks indicate statistical differences compared to DMSO and the color corresponds to the curve. Error bars represent the standard deviation. (**c**) Quantification of the root growth rate expressed in mm per hour of seedlings treated with DMSO, PD98059 and U0126 at 10µM for 12 hours. [two-way ANOVA followed by a post hoc Tukey HSD test; letters indicate statistical differences ($p<0.05$)]. Red crosses represent the average and the red bars the median. Black dots individual measurements.